



Discovery of oscillations in rotational speed of body-tethered *Caulobacter crescentus*Jordan Bell, George Araujo, and Jay X. Tang ^{*}*Department of Physics, Brown University, Providence, Rhode Island 02912, USA* (Received 12 June 2018; revised 29 October 2020; accepted 9 November 2020; published 14 December 2020)

Swarmer cells of *Caulobacter crescentus* have been found to tether to glass at a point on the cell body. The rolling of the freely rotating flagellum near the glass surface causes the cell body to rotate. We describe the discovery of damped oscillations in the rotational speed of these cell bodies. We show that the damped oscillations are robust over multiple cells and that they depend more on the cell's accumulated rotation angle than on time. We also find that their phase is determined by the moment the flagellar motor changes the direction of its rotation. The oscillations occur only for one direction of cell rotation, when the flagellum is in pulling mode. We discuss possible explanations for these oscillations, including fluctuations in flagellar motor torque and periodic changes in flagellar orientation, and illustrate both of these cases using simplified computer models. Finally, we present the hypothesis that the oscillations are the result of fluctuations in the proton motive force, initiated by a sudden change in proton current that occurs when the motor switches rotation direction.

DOI: [10.1103/PhysRevE.102.062416](https://doi.org/10.1103/PhysRevE.102.062416)**I. INTRODUCTION**

Caulobacter crescentus is a gram-negative bacterium commonly found in soil and freshwater. It is studied as a model organism for its dimorphic life cycle: A young cell has a single flagellum rotated by a molecular motor and swims around before maturing, losing its flagellum, and forming a stalk and holdfast structure to strongly anchor itself to a surface [1]. The mature form, called a “stalked cell,” periodically enters into predivisional stage and then buds off a swarmer cell every couple of hours [2,3]. The flagellum of the *C. crescentus* swarmer cell has a stable structure as a right-handed helix whether pushing or pulling the cell, as the motor rotates clockwise (CW) or counterclockwise (CCW), respectively, when viewed from the flagellum [4]. The flagellum is not observed to undergo polymorphic transformation like those of *Escherichia coli* [5]. The motor itself is powered by the inward flow of protons (H^+ ions) across the cell's inner membrane, shown in Fig. 1.

As has been shown recently [5], *Caulobacter* cells are able to tether to surfaces at points on the cell body. They are able to sense when they are adhered to a surface, possibly by the reduction of flagellar rotation leading to diminished proton flux through the motor [6], and skip ahead in their life cycles to form holdfast structures sooner than they would otherwise [7,8]. If there is a single point of attachment between the cell body and the solid surface, then the rolling of the free flagellum near the surface can cause the cell body to rotate with respect to the tether (see supplemental video 1 [9]). This tethering configuration has been used to draw conclusions about the *Caulobacter* motor's torque [5] and its direction-switching statistics [10]. Unlike the well-studied motor of *E. coli*, the *Caulobacter* motor produces torque asymmetrically—about twice as much CCW (flagellum pulling the cell body) as CW (flagellum pushing the cell body) [5]. It is unknown

whether this disparity is caused by higher fuel consumption in the CCW case or higher fuel efficiency. We will discuss potential arguments for the former case, as perturbations in proton flux might lead to oscillations in the proton motive force (pmf).

We describe the motion of the bacterium as illustrated in Fig. 2. The rotational velocity of the free flagellum is denoted $\bar{\omega}_F$. The torque on the cell body $\bar{\tau}_B$ is caused by a wall effect, an increased effective viscosity which can be considered a decaying function of distance from the wall, approaching the bulk viscosity for large distances. (This is a variation of the effect that causes bacteria with rotating flagella to swim in curved paths near a solid surface [11].) Portions of the flagellum that are closer to the wall experience higher drag. This asymmetric drag leads to a net torque about \hat{r}_B , causing the cell body to rotate with angular velocity $\bar{\omega}_B$ with respect to the tether. The cell's motor stochastically switches between intervals of CW and CCW rotation. By our convention (shown in Fig. 2), CCW motor rotation results in positive values for $\bar{\omega}_F$ and $\bar{\omega}_B$, so we refer to CCW intervals as positive and CW motor intervals as negative.

Here we discuss the discovery of large oscillations in $\bar{\omega}_B$, distinct in several ways from oscillations reported for tethered *E. coli* [12], and characterized by several robust attributes, which are observed across hundreds of flagellar motor switching events and tens of cells:

- (1) Dramatic oscillations appear only during intervals of positive rotation.
- (2) They are uncorrelated to the laboratory frame.
- (3) They are primarily a function of the angle the cell rotates rather than of time.
- (4) Their phase is set relative to the position of the cell at the moment of motor reversal.
- (5) They gradually damp out over tens of radians in $\bar{\theta}_B$.
- (6) When compared over multiple cells, larger oscillation amplitudes are observed for cells with faster rotation.

^{*}jay_tang@brown.edu

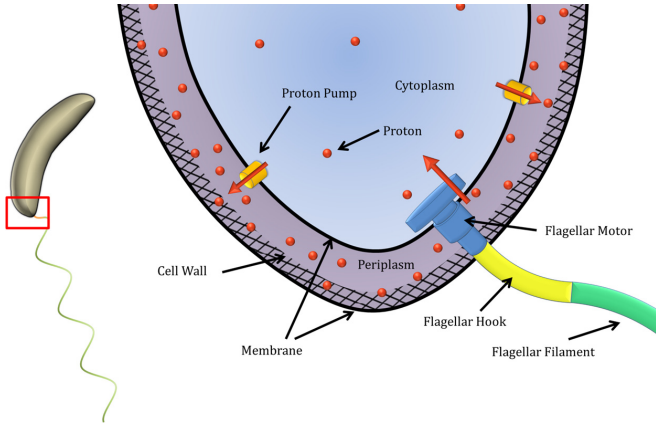


FIG. 1. Magnified schematic view of the flagellar polar region indicated by the red box. Proton flux is indicated by red arrows. The cell expends energy to pump protons from the inner cytoplasmic volume (within the inner membrane) to the periplasmic space (between the inner and outer membrane). The surplus of protons in the periplasm then acts as a reservoir of energy for cellular processes, including the rotation of the flagellar motor, which is powered as protons flow back into the cytoplasm. The proton motive force (pmf) causes the protons to return to the cytoplasm, and consists both a concentration gradient and an electric potential difference across the inner membrane.

These characteristics of the oscillations provide clues to their cause. Notably, they lack symmetry relative to rotation reversal, damping out and appearing for only one direction of rotation. Low-Reynolds number hydrodynamics dictates that objects and regions of fluid retrace their paths as driving forces reverse direction [13]. If the oscillations we observe were caused by purely hydrodynamic motion of the cell body or the flagellum, then that motion (and accompanying oscillation) would be expected for both directions of rotation. The fact that the motion does not obey low-Reynolds time reversibility thus indicates either a direction-dependent change in the cell's configuration (e.g., a mechanical instability that occurs in one direction but not the other) or an oscillatory variation in motor speed.

We first investigate whether the oscillations might be caused by changes in the angle the flagellum makes with respect to the cell body or the glass surface. These motions would alter the torque exerted on the cell body and result in changes to the speed of the cell's sweeping rotation. The question is whether the magnitude of such changes would match observations. The second type of mechanism, in which we envision "delayed control of pmf," produces oscillations in the cell's proton motive force (pmf) as the cell responds to higher proton current during the faster CCW motor rotation (see Fig. 1). The rotation rate of flagellar motors is proportional to pmf [14], and a lag in the cell's effort to control the pmf could lead to oscillations in both pmf and motor speed, as we will demonstrate.

II. METHODS

A. Cell culture

A pilless strain of *C. crescentus* (CB15 YB375- Δ pilin) was grown from freezer stock on 1.5% agar gel plates con-

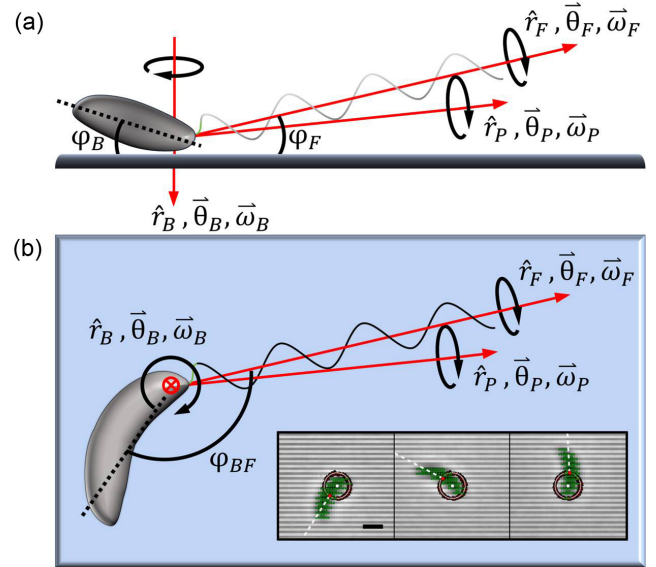


FIG. 2. Schematics of the rotating cell, in a frame of reference that is corotating with the cell and flagellum about the \hat{r}_B axis. (a) Side-on illustration of body-tethered *Caulobacter*. (b) Top-down view of the tethered cell. We describe the position of the cell using rotational (θ) and configurational (φ) angles. The angles of the cell body and the flagellum relative to the plane of the glass surface are given by φ_B and φ_F . The angle they make relative to each other when viewed from above is φ_{BF} . The unit vector \hat{r}_B is perpendicular to the glass, and points toward the glass through the point of the cell's attachment. The unit vector \hat{r}_F points from the flagellar motor along the flagellum's length. The angular displacements and velocities of the flagellum are given by $\bar{\theta}_F$ and $\bar{\omega}_F$, while those of the cell body are denoted $\bar{\theta}_B$ and $\bar{\omega}_B$. Three hypothesized flagellar motions are considered in this work. The "whirling" of the flagellum described in this report is a relatively slow gyration of the rapidly rotating filament's axis \hat{r}_F about another axis \hat{r}_P . The "cone angle" referred to in the text is the angle between \hat{r}_F and \hat{r}_P . The angular position and rate of the whirling is described by $\bar{\theta}_P$ and $\bar{\omega}_P$. The "swinging" flagellum is a planar oscillation of the angle φ_{BF} , while "lifting" is a planar oscillation of φ_F . Inset: Three video frames of body-tethered *Caulobacter* spaced 0.04 s apart (see the supplemental material [9]). Scale bar is 1 μm . The long axis of the cell is shown in dashed white and the cell's pixels in green. The location of the pivot is a white point found by fitting a circle to the previous locations of the cell's centroid (red).

taining peptone yeast extract (PYE) nutrient medium and refrigerated. Colonies were picked from the plates and cultured in liquid PYE (0.2% peptone, 0.1% yeast extract, 1.2 mM MgSO_4 , 0.5 mM CaCl_2). Briefly, the culture contained in a petri plate was allowed to grow for 3 days at 30°C with periodic replacement of PYE and no shaking, in order to obtain a high number of cells adhered to the plate surface. Swarmer cells were obtained via the plate release method [15]. On rinsing the plate twice with deionized water, 1 ml of PYE was allowed to sit in the dish for 5 min to collect freshly divided swarmer cells. The PYE was then collected and diluted with fresh PYE as needed to achieve a low-enough cell density for individual cell imaging.

B. Image acquisition and analysis

Cells were imaged in the PYE growth medium on a Nikon TE 2000-U microscope under phase contrast using a 60 \times objective lens. Samples were searched by eye for rotating body-tethered cells which had adhered to the glass coverslip. Once a rotating cell had been identified, a small region of interest around the cell was selected for high-speed video recording until the cell detached and swam away or stopped rotating. Across multiple experiments, about 60 cells were recorded executing sweeping rotation, and 12 of these were selected for further analysis due to active rotation of sufficient duration (22–419 s), and multiple motor switching events. Typical positive rotation intervals were about 1 s in duration, while negative rotation intervals were about 2–3 s (see Ref. [10] for distributions). The low-resolution video segments were recorded at 125 and 500 fps with a fast camera (FASTCAM PCI-R2, Photron USA, Inc.).

Recorded videos were analyzed with a custom Python script. Pixels belonging to a rotating cell were identified using intensity and proximity thresholds. The coordinates of the cell's pixels were then subjected to principal component analysis in order to estimate the angles and lengths of the cell's axes, as well as the cell's centroid location. Instances of flagellar motor reversal were identified by noting the farthest angle a cell rotated in a given direction before rotation commenced in the other direction. Rotation intervals were inspected individually and those compromised by other cells swimming near the tethered cell were discarded in the analysis. Measurements of cell position and speed were equally spaced in time due to the camera's constant frame rate. Some of our results require plotting the rotation rate against accumulated angle rather than time. Because the cells' speed varied, the measurements were no longer equally spaced when plotted against the cumulative angular position of the cell. Before averaging the measurements taken for different motor intervals, we used linear interpolation to bin the data into equally spaced angular positions.

The cells' flagellar poles were determined by exploiting asymmetry in their swimming behavior. *Caulobacter* swarmer cells manifest distinct trajectories for forward and backward swimming. They perform "flicking" maneuvers similar to some other unflagellated bacteria [16,17], leading to changes in swimming direction as the cell switches to swimming with the cell body leading. When the cells swim near a solid surface, their trajectories curve when the flagellum is leading the cell body [10]. By observing swimming cells before they adhere and after they detach from a glass coverslip, we determined that they tend to tether at points on the cell body near the flagellar pole. Wild-type cells were soon arrested by the attachment of multiple pili to the surface, but pililess mutants were observed to rotate nearly parallel to the glass ($\varphi_B < 20^\circ$, as determined by the length of the cell's projection) for periods as long as several minutes before detaching or becoming immobilized.

III. RESULTS

The flagellar motors of body-tethered cells switch back and forth between positive (CCW, $\bar{\omega}_F > 0$, flagellum pulling)

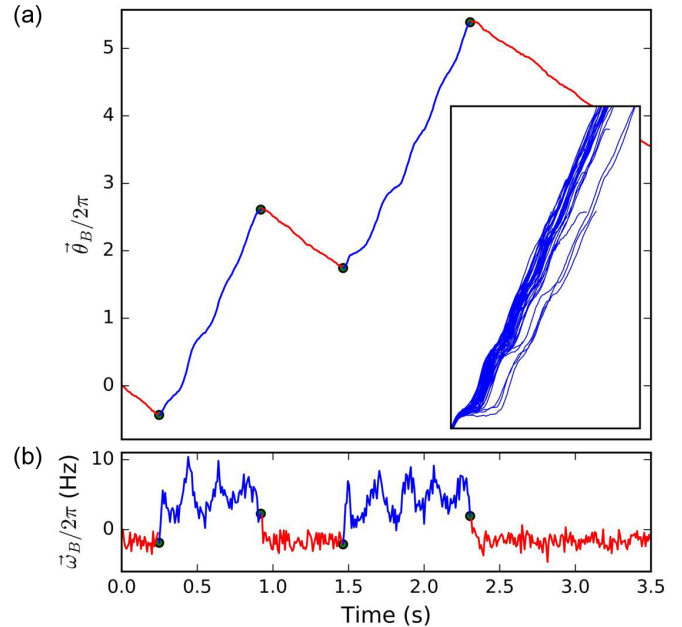


FIG. 3. (a) Cell body angular displacement ($\bar{\theta}_B$) vs. time for a body-tethered *Caulobacter* cell. Blue traces indicate positive intervals, while red indicates negative rotation and moments of motor reversal are indicated by green points. Inset: A collection of 50 positive intervals for this cell are shown with the same scale as those in the main panel, shifted to begin at the same point. (b) Rotational velocity ($\bar{\omega}_B$) of the cell body corresponding to the $\bar{\theta}_B$ traces in the main panel above.

and negative (CW, $\bar{\omega}_F < 0$, flagellum pushing) states. Due to interaction with the glass surface, positive $\bar{\omega}_F$ leads to a positive torque on the cell body ($\bar{\tau}_B$).

When the motors of rotating body-tethered cells switch from negative $\bar{\omega}_F$ to positive $\bar{\omega}_F$, $\bar{\omega}_B$ likewise switches from negative to positive. We refer to this as the CW-CCW switch, following the convention for the motor. Immediately following these events, we observed dramatic oscillations in $\bar{\omega}_B$ as shown in Fig. 3. We did not detect such oscillations when the tethered cells switched back to negative rotation. The oscillations were accompanied by only slight and inconsistent changes in φ_B as revealed by changes in the length of the cell's projection and were present even for cells tethered near the midpoint of their body, indicating that oscillation was not caused by variations in the tilt of the cell body. They also did not correlate with the laboratory frame, suggesting that they are not caused by anisotropic friction of the glass surface (e.g., a sticky spot). Their phase was set by the moment of the CW-CCW switch and usually began with a brief maximum in $\bar{\omega}_B$. The oscillations then typically decreased in amplitude until the cell body rotated at a constant speed after 5–10 revolutions.

We found it convenient to introduce coordinates for time and $\bar{\theta}_B$ that are relative to the time and position of the cell body at the moment of the CW-CCW switch. We call these coordinates t' and $\bar{\theta}_{B'}$. As shown in Fig. 4, we found that plotting the rotational velocity $\bar{\omega}_B$ of the positive intervals against $\bar{\theta}_{B'}$ rather than t' causes the oscillations to collapse into a master curve. We confirmed this by comparing the average

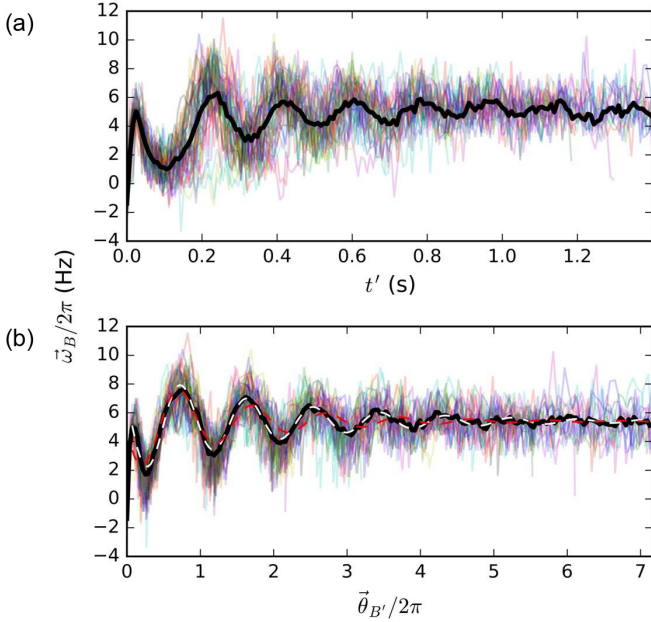


FIG. 4. (a) Rotational speed traces plotted against time from the moment of the CW-CCW switch (t') for 50 positive intervals for the cell featured in Fig. 3. Their average is indicated in black. (b) The same data as above but plotted against the angular displacement from the angle of the CW-CCW switch ($\bar{\theta}_{B'}$). The average is again shown in black. The white dashed line is a fit of the average (excluding the first two points) to the damped sinusoidal model with free parameters (α : -22.99 rad/s, β : 1.11, γ : 1.98 rad, δ : 0.08, ϵ : 33.99 rad/s, RMSE: 8.98 rad/s). The red dashed line illustrates the fit with the frequency parameter β constrained to 1 (α : -22.31 rad/s, β : 1.00, γ : 1.39 rad, δ : 0.11, ϵ : 33.99 rad/s, RMSE: 20.04 rad/s).

pairwise Pearson correlation coefficient of the rotational speed of positive intervals when parametrized by $\bar{\theta}_{B'}$ ($\bar{r} = 0.75$) and t' ($\bar{r} = 0.55$).

The form of the averaged speed oscillations begs comparison with the equation for a damped sinusoid. In order to characterize the oscillations, we fit our data with a damped sinusoidal model of the following form:

$$\omega_B = \alpha \sin(\beta\theta_{B'} + \gamma)e^{-\delta\theta_{B'}} + \epsilon, \quad (1)$$

where ω_B is the rotational speed in rad/s, α is the amplitude, β the frequency, γ the phase offset, δ the damping coefficient, and ϵ the steady-state rotational speed. Figure 4 demonstrates this model fit. Because the period of the oscillations for this cell is relatively close to one full rotation of the cell body, we include a damped sinusoidal fit of the data with the β parameter fixed at the value 1 in order to demonstrate that the data will not reasonably allow such a choice. Further demonstration of this fact is given in Fig. 5(a). We also note that the amplitude of the oscillations is sometimes so great that the cell is brought nearly motionless or even briefly rotated in the negative direction, particularly in the first trough.

The fact that the period of oscillation for the cells is so near 2π ($\beta = 1$) is one of their most conspicuous aspects. It certainly seems to be more than mere coincidence. Yet each cell has a different period and can be clearly shown to be different from 2π , as Fig. 5(a) reiterates. Furthermore, this tethering configuration, is completely symmetric about the axis of sweeping rotation \hat{r}_B —the cell has no way of directly tracking its progress about \hat{r}_B , and \hat{r}_B must be perpendicular to the surface without a rigid tether structure to support the cell. Finally, while we find that the oscillations are inherently related to the position at which the cell switches to positive rotation, we find no relationship between the locations where these switches occur and the laboratory frame. This is demonstrated in Fig. 5(b).

While we have followed the results for a single cell in Figs. 3–5, we observed similar behavior for 11 other cells that remained tethered, motile, and switching for sufficient data to

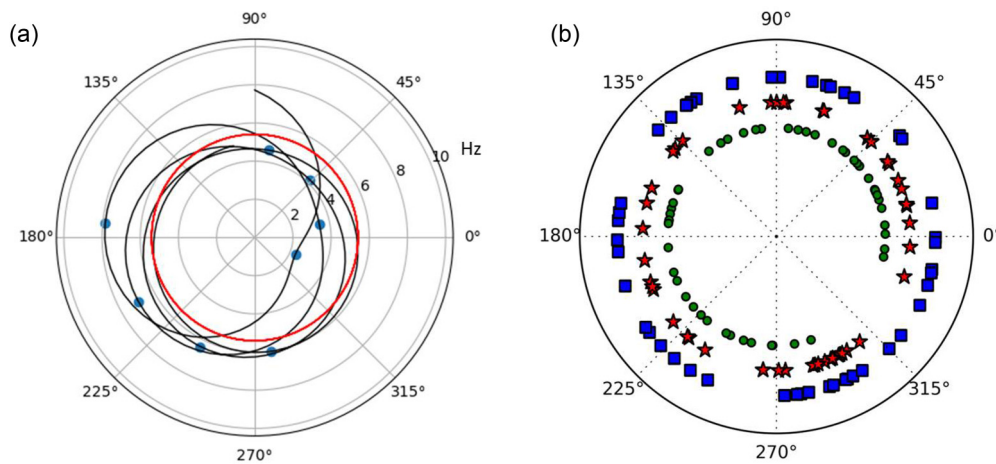


FIG. 5. Results demonstrating that the rotational speed oscillations do not have a period of one revolution and are not correlated to the laboratory frame. (a) A polar plot of the damped sinusoidal fit of observed body-sweeping rotational speed as depicted in Fig. 4, main text. The rotational speed of the cell body is plotted radially against the cell body's angular position. The position of the cell body at the moment of motor reversal is set at 90° . The speed of rotation oscillates as the cell body rotates clockwise (positive sweeping body rotation $\bar{\omega}_B$ as defined in Fig. 2), with local minima and maxima marked. The red circle represents the steady-state rotation rate. (b) A polar plot of the angular positions (lab frame) of the 50 CW-CCW switches (green circles) and 50 CCW-CW switches (red stars) observed for the cell featured in Figs. 3 and 4. A series of 50 random numbers is plotted for comparison (blue squares).

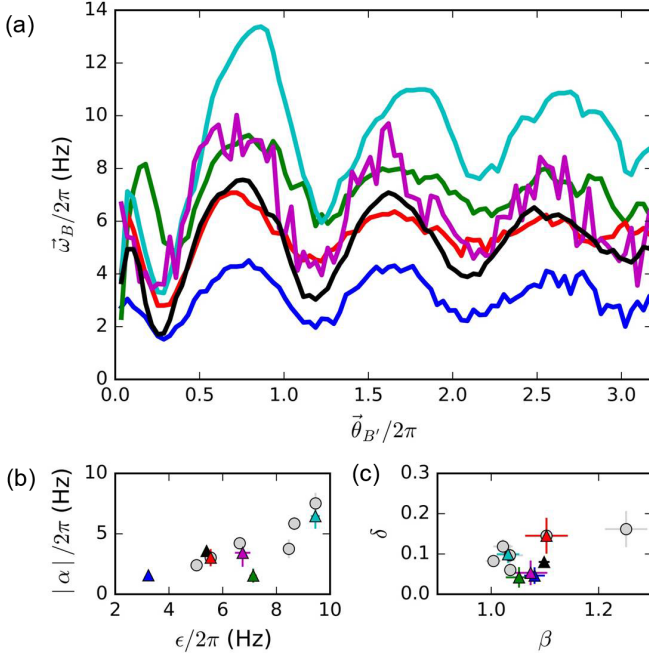


FIG. 6. (a) Average positive rotational velocity $\bar{\omega}_B$ traces for six representative cells plotted against the angular displacement from the point of switch ($\bar{\theta}_{B'}$). The black trace is that of the same cell featured in Figs. 3 and 4. (b) Damped sinusoidal fit parameters of the amplitude $|\alpha|$ plotted against the steady-state offset ϵ for 12 cells. Error bars [in both (b) and (c)] are 3 times the standard deviation (3σ) obtained from the covariance matrix of the least-squares fit. Triangle markers in matching colors are used for the points corresponding to the six cells of panel (a). (c) Damped sinusoidal best fit parameters [see Eq. (1)] for the damping constant δ plotted against the frequency β . Points representing those cells featured in panel (a) are again marked as triangles with colors that match the traces in (a).

be collected. Examples of rotational velocity oscillations for several cells are given in Fig. 6. The important fit parameters are also presented for all 12 cells. We find that the amplitude of the oscillations α increases with the cells' steady-state rotational speed ϵ . A linear fit of these data through the origin returned a value of 0.58 for the ratio of $|\alpha|$ to ϵ ($R^2 = 0.62$).

Using computer modeling, we investigated two alternative potential causes of the oscillation that are consistent with Figs. 6(b) and 6(c). The first is a change in the configuration of the flagellum relative to the cell body and the glass surface. The second is a change in motor torque output due to changes in pmf. These cases are treated under “Discussion.” We also considered additional mechanisms that could create oscillation. Variation in the resistance imparted by the tether (such as the super coiling of a fiber) might cause angle-dependent oscillation, but such a torque would not likely be dependent on the rotational rate of the cells as we observe. Cells were observed to accumulate hundreds of revolutions in each direction without any evidence of coiling or significant changes in resistance. It is also true that a mechanism other than pmf could be affecting motor torque. Both motor switching and stator remodeling affect torque, but generally on timescales that are too long or too short to be involved in these oscillations

[18–24]. We do not investigate this direction further in this work.

IV. DISCUSSION

At low Reynolds number, the rotational speed of a body is directly proportional to applied torque. In this case, the torque applied to the cell body τ_B is proportional to the speed at which the flagellum rotates:

$$\tau_B = D(\varphi_F, \varphi_{BF}) \omega_F, \quad (2)$$

where D is a scalar draglike coefficient that is a function of the angles the flagellum makes with the glass surface (φ_F) and the cell body (φ_{BF}). The angular velocity $\bar{\omega}_B$ of the cell body about its pivot is in turn a function of τ_B :

$$\bar{\omega}_B = M(\varphi_B) \bar{\tau}_B, \quad (3)$$

where a scalar mobility coefficient M is a function of the cell body's angle to the glass (φ_B), its physical dimensions, and any torsional resistance from the tether itself. Our approach to calculating D and M for the simulated flagellum models is discussed in sub section 1 of Appendix. We combine Eqs. (2) and (3) as:

$$\omega_B = M(\varphi_B) D(\varphi_F, \varphi_{BF}) \omega_F. \quad (4)$$

The oscillations that we observe in ω_B must therefore be caused by oscillations in M , D , and/or ω_F . It is especially interesting that the oscillations demonstrate a relationship between amplitude (α) and steady-state speed (ϵ) over multiple cells. The cells are tethered at various points along their bodies, and their bodies vary in length. Both the tethering location and length of the cells change their mobility coefficients (M) and are assumed to be independent of motor or flagellar characteristics. The fact that a relationship between $|\alpha|$ and ϵ remains over randomized rotational drag suggests that the cause of the oscillation is the same as the cause of rotation or closely linked to it, eliminating contradictory hypotheses. The data also suggest that the rotational speed of the cell ω_B is tied to the angle $\bar{\theta}_{B'}$ the cell has rotated since the CW-CCW switch. There must be a link between the two—a way for the cell to know how far it has rotated since the motor switching event. To maintain relatively coherent angle-dependent oscillations for multiple cells with different rotation speeds, the link must be largely time-independent and have a memory relatively robust to thermal noise.

A. Periodic motion of the flagellar axis

The first explanation is that the angular distance the cell has traveled may be correlated to the motion of its flagellar axis \hat{r}_F . Such an angular dependence (rather than time dependence) has been observed for flagellar bundling for freely swimming multiflagellated bacteria [25]. But why would there be oscillation in the position of the flagellum relative to the cell body? The system as a whole is extremely overdamped, stopping instantaneously when a driving force ceases. While we do consider planar oscillatory motions of the flagellum in the angles φ_{BF} and φ_F separately, it is difficult to imagine a cause for strictly planar oscillation. An overdamped decay to an equilibrium position seems a much more realistic result of

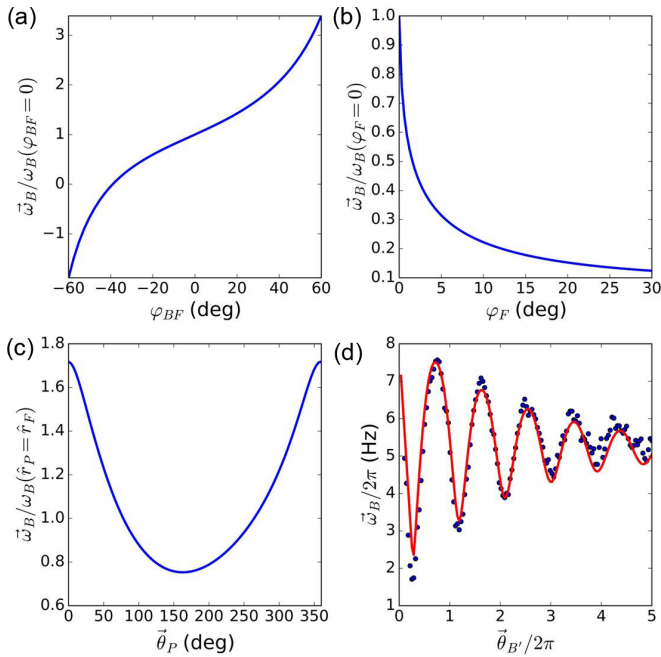


FIG. 7. Results of calculations investigating potential causes of the observed oscillations. (a) Predicted change in cell rotation due to changes in φ_{BF} . The predicted rotation rates are normalized to the case where the flagellum extends radially from the center of rotation. A leading flagellum imparts more torque to the cell, while a severely lagging flagellum would pull the cell backwards. The distance from the motor to the tether point is accounted for. (b) Predicted change in cell rotation speed for varying values of φ_F . Values are normalized to the case in which the flagellum is parallel to the glass ($\varphi_f = 0$). The torque exerted on the cell is predicted to drop drastically as the flagellum lifts from the surface. (c) Predicted speeds of cell rotation for a whirling flagellum—a flagellum sweeping out a cone. The speeds are normalized to the case where the flagellum is stable along the cone’s axis and are plotted against the azimuthal angle $\hat{\theta}_P$. The cone angle (angle between \hat{r}_P and \hat{r}_F) is set at 1° . The angle $\hat{\theta}_P$ is set to zero when the flagellum is parallel to and closest to the solid surface, and 90° at maximum lagging. The φ_F component dominates over the φ_{BF} component, resulting in maximum speed when the flagellum is nearest the surface. (d) Results of a pmf control simulation are plotted against experimental data from our featured cell. In this model, the flagellar configuration does not change. The cell acts with a delay of 60 ms to counteract a sudden decrease in pmf caused by a larger motor proton flux for CCW motor rotation. The delay leads to overcorrection and subsequent oscillation in motor torque. The model fits the data very cleanly, including peaks that are more rounded than the troughs.

any perturbation to these angles. One possibility is a periodic motion that is driven by the rotation of the motor, such as the “whirling” motion predicted by some models [26–28].

We separately investigate the effect of three changes in flagellar configuration on the tangential force imparted to the cell: a “swinging” back and forth about an equilibrium φ_{BF} value, a “lifting” up and down about an equilibrium φ_F value, and a “whirling” of \hat{r}_F about \hat{r}_P that is a combination of swinging and lifting. We present the results in Figs. 7(a)–7(c) and more details in sub section 1 of Appendix. As found earlier in Fig. 6, the typical maximum amplitude for the

oscillations is about 0.58 times the value of the steady-state sweeping rotation rate. The results of the calculation suggest that this amount of variation might be expected for a swinging flagellum that deviates about 25° from its equilibrium value. The tangential force the flagellum applies to the cell is much more sensitive to “lifting” in our simulation, requiring only about 1° to cause the same amount of variation. Likewise, we find that a cone angle on the order of only 1° would be sufficient in the whirling model.

We consider it highly unlikely that angles as small as those predicted for the lifting and whirling models would persist long enough under Brownian motion to be relevant to the observed oscillations (see, for example, the supplemental information to Ref. [17]). If the trajectory of the flagellum were responsible for the oscillations, then knocking the flagellum off track would quickly destroy their coherence.

B. PMF oscillation model

Oscillations in the actual torque produced by the flagellar motor would also lead to an increase in $|\alpha|$ with increasing ϵ , without requiring periodic deflection of the flagellum. After considering various ways that motor torque might vary, we feel that change in the pmf seems to match best with the timescale of the oscillations, though the model we discuss might apply to other ways in which the cell seeks to maintain a target motor speed.

The maintenance of pmf is a case study in process control. On average, the pumping of protons must balance the flow of protons back into the cytoplasm, including the contributions of adenosine triphosphate (ATP) synthase, the flagellar motor, and any leaks. If the higher torque of the motor in CCW mode is due to higher proton flux, then the moment of motor switching represents a step increase in proton flux to the cytoplasm that the cell must adapt to. Oscillations are easily obtained in such a system if the cell cannot respond instantaneously. We implemented a simple model to illustrate this, in which a 60-ms lag in the cell’s feedback loop is enough to cause oscillations with the same shape as the experimental data for our featured cell [Fig. 7(d)]. The data from the other cells can be fit with similar success, with an average lag time of 52 ms (± 18 ms SD). The details of the model are presented in sub section 2 of Appendix.

The proton motive force is the sum of two parts: a trans-membrane electric potential and a difference in pH (proton gradient). The proton gradient generally contributes less to the pmf (30–40%) [14,29]. In addition, buffering may keep the Δ pH component quite stable against perturbations. The buffering capacity of bacterial cytoplasm has been shown to be quite high, although perforating the membrane still causes rapid change in pH [30]. If a sudden change in the proton flux through the motor is in fact able to significantly affect the pmf, then it is more likely to do so through a change in the membrane potential. Significant variation in the membrane potentials of single cells has been observed in *E. coli*, using special proteins with potential-dependent fluorescence [31,32].

A lot of perspective is gained by considering how many protons are actually involved at any given moment. We can approximate this with estimates of periplasmic and cytoplas-

mic pH and the volume of our representative cell. We treat the cell as a prolate ellipsoid, with semi-major axes of lengths 1.3 and $0.25 \mu\text{m}$. We approximate the cytoplasm as a smaller ellipsoid within the outer membrane, such that there is a 25 nm periplasmic gap between the two. Using these dimensions, the volume of the cytoplasm is about 0.27 fl, and the volume of the periplasm is about 0.07 fl. Taking the approximation that the pH of the cytoplasm is 7.6 ($[\text{H}^+] = 25 \text{ nM}$) and that of the periplasm is 7.0 ($[\text{H}^+] = 100 \text{ nM}$) [29], we find that at any moment, there are roughly four free protons in the cytoplasm and four free protons in the periplasm. If the buffering capacity of *Caulobacter's* cytoplasm is as high as other bacterial species, however, then the available protons in the buffer could number in the hundreds of millions [30]. While the pH of the cytoplasm or periplasm may not change much, calculation of the Nernst potential for these concentrations suggests that the membrane potential could easily swing by 100 mV or more as a few hundred extra protons are transferred in either direction.

The rate at which *Caulobacter's* motor transports protons has not, to our knowledge, been quantified, but the flagellar motor of *Streptococcus* has been measured to use about 1200 protons per revolution [33]. Taking these numbers at face value, we find *Caulobacter* to use perhaps 10 000 protons per second for the motor alone, giving an idea of the turnover rate. A sudden change in the magnitude of proton flux at this rate could easily be expected to affect the membrane potential. Bacteria offset changes in membrane potential due to proton flux with transport of other ions (e.g., K^+), so transport of these other ions could play a role in the current case [34].

The pmf model can only succeed if the rotation rate of the motor affects the pmf in addition to being affected by the pmf. If this is the case, then changes in the pmf may be crucial for *Caulobacter's* ability to detect nearby surfaces and direct the just-in-time production of its holdfast structure. This ability has been attributed to interference with free flagellar rotation [7,8] but has been observed for mutants lacking flagella as well [6]. Either way, an intact motor is required, and the sensing of pH by DgcB has been suggested as a possible step in the communication between the motor and the holdfast secretion apparatus [6].

Oscillations like those we observe for *Caulobacter* can be found in suboptimally tuned proportional-integral-derivative [35] control systems, resulting from lags in the system. The phenomenon might also be modeled as a transmembrane inductance, as a component of a membrane or electric circuit analogy. While the adaptation of the cell's respiration [29,36] may somehow lag the pmf directly (hysteresis), it is more likely to lag in time, leading to the introduction of some time dependence for the cells' rotational speed. Because the cells rotate at different speeds, and the same cell may rotate at slightly different speeds for different intervals of positive rotation, a large time dependence would destroy the angle-coherence observed for the oscillations, but it turns out that a small time dependence actually fits the observations better. Because the pmf model has some dependence on time, plotting against the accumulated angle leads to peaks that are more rounded than the troughs. This effect is actually noticeable in the experimental data (Fig. 6). The degree to which this effect is seen in our pmf simulations depends on the relative magnitudes of α and ϵ .

Further evidence of some time dependence is found in the fact that the collapse of the data as shown in Fig. 4 is slightly but significantly more complete when the rotational speed data are plotted against a combination of time and accumulated angle, rather than only one of the two. For example, the speed traces of the positive intervals of our representative cell actually collapse best when plotted against a parameter of $(t')^{0.3}(\bar{\theta}_B)^{0.7}$. This mixture of time and angle gives an average Pearson correlation coefficient of $\bar{r} = 0.78$ between pairs of positive intervals, while plotting only against t' gave $\bar{r} = 0.55$ and plotting only against $\bar{\theta}_B$ gave $\bar{r} = 0.75$. Although small, the difference between $\bar{r} = 0.78$ and $\bar{r} = 0.75$ is highly significant ($p = 4 * 10^{-56}$, paired two-tailed t test). The speed oscillations for other cells also collapse more completely when plotted against a mix of time and angle, though the combination varies somewhat between $(t')^{0.5}(\bar{\theta}_B)^{0.5}$ and $(t')^{0.1}(\bar{\theta}_B)^{0.9}$.

The maintenance of the pmf is complex and is intricately tied to cellular respiration (the electron transport chain) [37,38], studied most extensively for the mitochondria of eukaryotic cells. The pumping of protons by the electron transport chain is dependent on the available concentrations of various entities, including oxygen, adenosine diphosphate (ADP), nicotinamide adenine dinucleotide phosphate (NADH), and cytochrome *c*, and deficiencies of one or more ingredients will affect the respiratory state of the mitochondrion or bacterium. With the complexity of cellular respiration, and little information about the respiration of *Caulobacter* in particular, there could easily be multiple sources of lag in a cell's adaptation to a sudden change in pmf. It has been shown that some bacteria are able to compensate for a decrease in one component of pmf (membrane potential or ΔpH) by controlling another [39], but this process takes minutes, far too long to account for the oscillations we observe. A much faster possibility involves ATP synthase, the proton-powered rotary enzyme responsible for ATP production in living cells. Under normal operating conditions, i.e., a sufficiently high pmf, ATP synthase transmits protons across the membrane, phosphorylating ADP. On a drop in the membrane potential, the enzyme operates in reverse as F_0F_1 -ATPase, utilizing the energy of ATP to pump protons backwards and shore up the pmf. This behavior is responsible for a prolonged maintenance of the pmf on cessation of respiratory proton pumping. It is conceivable that the reverse operation of ATP synthase as F_0F_1 -ATPase would be the method that a healthy *Caulobacter* cell would employ to counteract a motor that suddenly began leaking protons at a much higher rate. An experiment on mitochondria found that the pH difference between the inner and outer membranes temporarily overshoot the equilibrium value when cells were suddenly supplied with oxygen after it had been denied for 2 min [40]. A subsequent mathematical model concluded that this overshoot was attributable to a delay in reversal of F_0F_1 -ATPase such that the system adapted only after a lag period of 80 ms [41]. The pmf model presented here reproduces the observed oscillations in precisely the same way. A delay in the pmf control leads to an overshoot, and the characteristic delay times we measure (52 ms on average) are very similar to the 80 ms delay found for F_0F_1 -ATPase.

The hypothesis that the oscillations are caused by a lag in the response of ATP synthase or F_0F_1 -ATPase also suggests a simple explanation for why the oscillations appear only for positive intervals. When the motor switches back to slow mode and the equilibrium pmf rises to normal levels, ATP synthase no longer assumes its pumping function, and the proton gradient is maintained solely by respiration once again. Despite differences between prokaryotes and mitochondria [42], the parallels with mitochondria convince us that oscillations in pmf are interesting as a hypothetical explanation for our observations.

A promising route for testing of the pmf conjecture may be to take direct control of the pmf, perhaps by changing oxygen availability or using ionophores such as indole or butanol [43]. A more elaborate approach might utilize light-sensitive proton pumps such as proteorhodopsin [44]. Altering proton pumping or leaking would alter the observed waveforms in ways our pmf model might predict and which the whirling flagellum model could not account for. Sophisticated tracking of swimming cells may also prove useful in testing the two proposals [45].

V. CONCLUSION

By physical arguments and careful data analysis, we have demonstrated aspects of observed oscillations in the rotational speed of body-tethered *Caulobacter* cells—a particularly robust and consistent phenomenon that, to our knowledge, is novel among bacterial species. We have suggested possible mechanisms for the phenomenon and have explored their feasibility with computer modeling. More experimental evidence is required in order to determine whether one of these mechanisms is correct.

We find these oscillations fascinating and worthy of further study. If flagellar dynamics are responsible, then they provide an interesting hydrodynamic problem. If changes in pmf are responsible, then they may provide a new window into bacterial respiration and electrophysiology. The discovery of some other mechanism may be equally interesting.

ACKNOWLEDGMENTS

We are grateful to Thomas Powers for helpful discussions and Yves Brun for the strains used in the study. The work was supported by NSF CBET 1438033.

APPENDIX

1. Whirling flagellum model

The torque τ_B that causes the cell body to sweep around its tether is produced by a flagellum that is both pulling along its axis and feeling increased drag near the glass, in a motion similar to rolling. The force produced by the flagellum is transferred to the cell body at the location of the motor, and includes a component tangential to the cell's sweeping rotation. The magnitude of this component determines the cell's sweeping speed, and is affected by both the angle the flagellum makes with the cell body (φ_{BF}) and the angle it makes with the glass surface (φ_F). In addition, the drag force experienced by the flagellar helix due to the sweeping motion

depends on flagellar position, and must be accounted for. The aim of our first computer model is to estimate how much φ_B or φ_{BF} would need to deviate from their steady-state value in order to cause the magnitude of oscillations observed for the sweeping speed of the cells.

Our flagellar calculations are based on resistive force theory. We begin by investigating the relationship expressed by Eq. (2) in the main text. The torque magnitude τ_B is a product of the tangential force exerted by the flagellum at the cell pole and the distance of the flagellar pole from the point of rotation. The draglike coefficient $D(\varphi_F, \varphi_{BF})$ can then be split into this distance and a component that gives a force when multiplied by ω_F . The distance can be measured once the flagellar pole is known, but the force component requires calculation.

Our simulation calculates the force by integrating the drag experienced by each segment of a flagellum within a specified flow field. We chose to use the frame of reference of the flagellum, with the motor at the origin, and with fluid moving relative to the filament. The drag force experienced by a portion of the flagellum is dependent on the relative velocity of the fluid in its vicinity and the distance from its position to the solid surface. For the drag, we used the following approximation [11]:

$$f_{\parallel} = \frac{f_{\perp}}{2} = \frac{2\pi\mu}{\ln(2z/r)}. \quad (\text{A1})$$

Here f is the drag force per unit length for drag perpendicular or parallel to the flagellar segment, r is the radius of the flagellar filament, and z is the distance of the filament segment from the surface of the glass. The dynamic viscosity of water is given by μ . The force is then integrated over the entire flagellum to yield the total force acting on the bacterial cell at the point of the motor.

We specify the position vectors ($\vec{x}_1, \vec{x}_2, \vec{x}_3, \dots, \vec{x}_N$) and tangent vectors ($\vec{s}_1, \vec{s}_2, \vec{s}_3, \dots, \vec{s}_N$) for $N = 200$ segments of the flagellar helix, modeling each segment as a short straight rod. In our model, we used a $6\text{-}\mu\text{m}$ flagellum with helical radius of $0.28\text{ }\mu\text{m}$, pitch of $1.08\text{ }\mu\text{m}$ [4], flagellar filament radius of 7 nm , and cell body width of $0.5\text{ }\mu\text{m}$ as in Ref. [46]. We adopted a value of $0.29\text{ }\mu\text{m}$ for the distance from the motor to the glass surface, bringing the filament 10 nm from the glass surface at closest approach. We used rotation matrices to rotate \vec{x}_n and \vec{s}_n about the \hat{r}_B , \hat{r}_P , and \hat{r}_F axes. The major sources of fluid velocity relative to the filament are the rotation of the cell's motor ($\vec{v}_{F,n} = v_F \vec{x}_n \times \hat{r}_F$) and the sweeping rotation of the cell itself ($\vec{v}_{B,n} = v_B \vec{x}_n \times \hat{r}_B$). We neglected small contributions to the velocity due to whirling, swinging, or lifting.

The drag for each segment is dependent on the distance to the wall, and components of the fluid velocity perpendicular and parallel are handled separately as described by Eq. (A1). The force is then integrated over the entire flagellum to find the total force applied by the flagellum on the cell body at the point of the motor. Under Stokes drag, the forces on the cell at the location of the motor are balanced. The magnitude of the propulsive force from the "rolling" flagellum ($F_{\text{flag,propulsion}}$) must balance the magnitude of the flagellum's own drag ($F_{\text{flag,drag}}$) as well as that of the cell body ($F_{\text{body,drag}}$)

as they sweep through the fluid:

$$F_{\text{flag.propulsion}} = F_{\text{flag.drag}} + F_{\text{bodydrag}}. \quad (\text{A2})$$

We calculated $F_{\text{flag.drag}}$ by subjecting a nonrotating flagellum to a flow rotating around \hat{r}_B . We updated this estimate for each new flagellar position we studied. As with $F_{\text{flag.propulsion}}$ below, there is a small dependence on $\vec{\theta}_F$, so we average over a full rotation of the flagellum.

The drag term for the body is related to the mobility coefficient M from Eq. (3). We estimated F_{bodydrag} by modeling the cell body as a prolate ellipsoid with dimensions similar to those of our cells. The rotational drag of a prolate ellipsoid that is rotating about an off-center axis parallel to a minor axis can be calculated as a superposition of a rotation about and a translation along its minor axis [47–49]. We measured the distance from the center of the rotation to the flagellar pole to convert the rotational drag torque into an equivalent force F_{bodydrag} at the location of the motor. For our cells, the values of F_{bodydrag} and $F_{\text{flag.drag}}$ were similar on average, so we used the approximation that they were equal for our representative plot (Fig. 7).

In our calculation of $F_{\text{flag.propulsion}}$, we address the rotation about \hat{r}_F , but hold torque constant as observed for *Caulobacter*'s motor under similar loads [46]. We hold motor torque at 400 pN*nm and recalculate the motor rotation speed for each flagellar position as the drag changes with the distance to the wall.

Both the propulsive force of the rolling flagellum and its drag are affected by the flagellar configuration, while the drag of the cell body is not. The sweeping speed ω_{B1} of the whole cell when the flagellum is in a position 1 can be related to its speed ω_{B2} when the flagellum is in position 2 by:

$$\frac{\omega_{B1}}{\omega_{B2}} = \frac{F_{\text{bodydrag}} + F_{\text{flag.drag2}}}{F_{\text{bodydrag}} + F_{\text{flag.drag1}}} * \frac{F_{\text{flag.propulsion1}}}{F_{\text{flag.propulsion2}}}. \quad (\text{A3})$$

In the above equation, we allow negative values of F to represent forces in opposite directions, while in Fig. 7, we use the vector $\vec{\omega}_{B1}$ normalized to the magnitude ω_{B2} to handle negative values.

2. Delayed PMF adaptation model

The pmf consists of components corresponding to the proton gradient and membrane potential. In this model, we do not

distinguish between the two components. Because we assume that the rotational velocity of the cell ($\vec{\omega}_B$) is proportional to the pmf, we use a variable P that represents pmf directly, but is scaled to the same magnitude as the rotational speed of the cell in Hz. This allows us to fit the model to the data directly.

We start with the assumption that the proton currents that cause a decrease in P are proportional to P , in Ohm's law fashion. We call the rate constant R^- . The reduction in pmf in an interval of time Δt is $R^-(P)\Delta t$. If the motor passes more protons for CCW rotation than for CW rotation, then the value of R^- would suddenly increase with the CW-CCW motor switch.

In this simplified model, the cell performs proportional control of pmf, increasing P by an amount proportional to the difference from P to a target value P_0 . The rate constant is R^+ , and the increase in an interval of time is $R^+(P_0 - P)\Delta t$. The pmf will be stable when $R^+(P_0 - P) = R^-(P)$.

Oscillations can occur when there is a delay in the cell's control mechanism. If the cell does not react quickly enough to a change in P , then the value of P can overshoot the equilibrium value and result in oscillations. The model assumes that such a delay can be described by a single "effective lag time." Our pmf model is thus defined by the calculation of P at the n th time step:

$$P_n = \begin{cases} P_{\text{slow}}, & n < 0 \\ P_{n-1} + R^+(P_0 - P_{n-m})\Delta t - R^-(P_{n-1})\Delta t, & n > 0 \end{cases}, \quad (\text{A4})$$

where P_{slow} is the value of P before the CW-CCW switch and m is the number of time steps in the effective lag time. To fit the rotational speed data, we integrate P with respect to time, tracking the cell's cumulative rotation. Plotting P against this integrated value allows us to plot sinusoidal curves similar to those of the cell's speed.

We use least-squares fitting to find the most successful parameter values. We set the number of steps for the delay to $m = 100$, and fit the values of R^+ , R^- , P_0 , and Δt . The model fit in Fig. 7 was created using $R^+ = 37.8 \text{ s}^{-1}$, $R^- = 26.5 \text{ s}^{-1}$, $P_{\text{slow}} = 8.2$, $P_0 = 8.9$, and $\Delta t = 0.60 \text{ ms}$. Because the effective lag time consists of 100 time steps, we obtain a value of 60 ms for this delay.

-
- [1] P. H. Tsang, G. Li, Y. V. Brun, L. B. Freund, and J. X. Tang, *Proc. Natl. Acad. Sci. USA* **103**, 5764 (2006).
- [2] L. Shapiro, *Annu. Rev. Microbiol.* **30**, 377 (1976).
- [3] J. M. Skerker and M. T. Laub, *Nat. Rev. Microbiol.* **2**, 325 (2004).
- [4] S. Koyasu and Y. Shirakihara, *J. Mol. Biol.* **173**, 125 (1984).
- [5] P. P. Lele, T. Roland, A. Shrivastava, Y. Chen, and H. C. Berg, *Nat. Phys.* **12**, 175 (2016).
- [6] I. Hug, S. Deshpande, K. S. Sprecher, T. Pfohl, and U. Jenal, *Science* **358**, 531 (2017).
- [7] G. Li, P. J. B. Brown, J. X. Tang, J. Xu, E. M. Quardokus, C. Fuqua, and Y. V. Brun, *Mol. Microbiol.* **83**, 41 (2012).
- [8] C. Berne, C. K. Ellison, A. Ducret, and Y. V. Brun, *Nat. Rev. Microbiol.* **16**, 616 (2018).
- [9] See Supplemental Material <http://link.aps.org/supplemental/10.1103/PhysRevE.102.062416> for the raw video of the representative cell highlighted in the figures. An additional supplemental video is provided, which shows animated plots of rotational speed and cell size measurements for the featured cell.
- [10] M. Morse, J. Bell, G. Li, and J. X. Tang, *Phys. Rev. Lett.* **115**, 198103 (2015).
- [11] E. Lauga, W. R. DiLuzio, G. M. Whitesides, and H. A. Stone, *Biophys. J.* **90**, 400 (2006).

- [12] M. Kara-Ivanov, M. Eisenbach, and S. R. Caplan, *Biophys. J.* **69**, 250 (1995).
- [13] E. M. Purcell, *Am. J. Phys.* **45**, 3 (1977).
- [14] C. V. Gabel and H. C. Berg, *Proc. Natl. Acad. Sci. USA* **100**, 8748 (2003).
- [15] S. T. Degnen and A. Newton, *J. Mol. Biol.* **64**, 671 (1972).
- [16] L. Xie, T. Altindal, S. Chattopadhyay, and X.-L. Wu, *Proc. Natl. Acad. Sci. USA* **108**, 2246 (2011).
- [17] K. Son, J. S. Guasto, and R. Stocker, *Nat. Phys.* **9**, 494 (2013).
- [18] F. Bai, R. W. Branch, D. V. Nicolau, Jr., T. Pilizota, B. C. Steel, P. K. Maini, and R. M. Berry, *Science* **327**, 685 (2010).
- [19] E. A. Korobkova, T. Emonet, H. Park, and P. Cluzel, *Phys. Rev. Lett.* **96**, 058105 (2006).
- [20] H. C. Berg, *Protein Sci.* **26**, 1249 (2017).
- [21] R. Chawla, K. M. Ford, and P. P. Lele, *Sci. Rep.* **7**, 5565 (2017).
- [22] P. P. Lele, B. G. Hosu, and H. C. Berg, *Proc. Natl. Acad. Sci. USA* **110**, 11839 (2013).
- [23] N. Wadhwa, R. Phillips, and H. C. Berg, *Proc. Natl. Acad. Sci. USA* **116**, 11764 (2019).
- [24] J. A. Nirody, A. L. Nord, and R. M. Berry, *J. R. Soc. Interface* **16**, 20190300 (2019).
- [25] Z. Qu, F. Z. Temel, R. Henderikx, and K. S. Breuer, *Proc. Natl. Acad. Sci. USA* **115**, 1707 (2018).
- [26] C. W. Wolgemuth, T. R. Powers, and R. E. Goldstein, *Phys. Rev. Lett.* **84**, 1623 (2000).
- [27] Y. Park, Y. Kim, W. Ko, and S. Lim, *Phys. Rev. E* **95**, 022410 (2017).
- [28] M. Jabbarzadeh and H. C. Fu, *Phys. Rev. E* **97**, 012402 (2018).
- [29] J. L. Slonczewski, B. P. Rosen, J. R. Alger, and R. M. Macnab, *Proc. Natl. Acad. Sci. USA* **78**, 6271 (1981).
- [30] T. A. Krulwich, R. Agus, M. Schneier, and A. A. Guffanti, *J. Bacteriol.* **162**, 768 (1985).
- [31] J. M. Kralj, D. R. Hochbaum, A. D. Douglass, and A. E. Cohen, *Science* **333**, 345 (2011).
- [32] T. J. Zajdel, M. A. TerAvest, B. Rad, C. M. Ajo-Franklin, and M. M. Maharbiz, in *Proceedings of the 2014 IEEE Conference on Sensors (SENSORS'14)* (IEEE, Los Alamitos, CA, 2014), pp. 1764–1767.
- [33] M. Meister, G. Lowe, and H. C. Berg, *Cell* **49**, 643 (1987).
- [34] I. R. Booth, *Microbiol. Rev.* **49**, 359 (1985).
- [35] G. F. Franklin, J. D. Powell, and M. L. Workman, *Digital Control of Dynamic Systems*, Vol. 3 (Addison-Wesley, Menlo Park, CA, 1998).
- [36] T. A. Krulwich, G. Sachs, and E. Padan, *Nat. Rev. Microbiol.* **9**, 330 (2011).
- [37] Y. Anraku, *Annu. Rev. Biochem.* **57**, 101 (1988).
- [38] W. J. Ingledew and R. K. Poole, *Microbiol. Rev.* **48**, 222 (1984).
- [39] E. P. Bakker and W. E. Mangerich, *J. Bacteriol.* **147**, 820 (1981).
- [40] S. Ogawa and T. M. Lee, *J. Biol. Chem.* **259**, 10004 (1984).
- [41] H.-G. Holzhütter, W. Henke, W. Dubiel, and G. Gerber, *Biochim. Biophys. Acta* **810**, 252 (1985).
- [42] J. M. Benarroch and M. Asally, *Trends Microbiol.* **28**, 304 (2020).
- [43] E. Krasnopeeva, C.-J. Lo, and T. Pilizota, *Biophys. J.* **116**, 2390 (2019).
- [44] J. M. Walter, D. Greenfield, C. Bustamante, and J. Liphardt, *Proc. Natl. Acad. Sci. USA* **104**, 2408 (2007).
- [45] B. Liu, M. Gulino, M. Morse, J. X. Tang, T. R. Powers, and K. S. Breuer, *Proc. Natl. Acad. Sci. USA* **111**, 11252 (2014).
- [46] G. Li and J. X. Tang, *Biophys. J.* **91**, 2726 (2006).
- [47] V. A. Bloomfield, *Separations and Hydrodynamics*, edited by T. M. Schuster (Biophysical Society, Rockville, MD, 2000), Chap. 1, pp. 7–8.
- [48] C. R. Cantor and P. R. Schimmel, *Biophysical Chemistry Part II: Techniques for the Study of Biological Structure and Function*, 1st ed. (W. H. Freeman and Company, London, 1980), pp. 560–563.
- [49] J. Happel and H. Brenner, *Low Reynolds Number Hydrodynamics* (Martinus Nijhoff, The Hague, The Netherlands, 1983), pp. 222–224.